Plasma Chem Plasma Process (2010) 30:907–931
DOI 10.1007/s11090-010-9254-3

ORIGINAL PAPER

Simulation of Excimer Ultraviolet (EUV) Emission from a Coaxial Xenon Excimer Ultraviolet Lamp Driven by Distorted Bipolar Square Voltages

S.-Y. Jou · C.-T. Hung · Y.-M. Chiu · J.-S. Wu · B.-Y. Wei

Received: 18 August 2010 / Accepted: 22 September 2010 / Published online: 2 October 2010

Abstract Simulation of excimer ultraviolet (EUV) emission from a coaxial xenon excimer ultraviolet lamp driven by distorted bipolar square voltages is presented in this study. A self-consistent radial one-dimensional fluid model, considering local mean energy approximation (LMEA), along with a set of simplified xenon plasma chemistry was employed to simulate the discharge physics and chemistry. Emitted powers of EUV light and deposited powers to the charged species were simulated by varying the values of four key parameters, which include the driving frequency, gas pressure, gap distance and number of dielectric layers. Results show that there are three distinct periods that include pre-discharge, discharge and post-discharge ones. It is found that intensive EUV (172 nm) emission occurs during the early part of the discharge period, which correlates very well in time with the power deposition through electrons. In addition, power deposition through Xe^+ and Xe_2^+ occurs mainly in the discharge period and later part of discharge period, respectively. Surprisingly, the emission efficiency of 172 nm increases slightly with increasing driving frequency of power source, while it increases dramatically with increasing gap distance. In addition, the maximal emission efficiency is found to take place at gas pressure of 600 torr. The emission efficiency of one-dielectric case is found to be better than that of two-dielectric one. The underlying mechanisms in the above observations are discussed in detail in the paper.

Keywords Coaxial xenon excimer lamp · Excimer ultraviolet · Fluid modeling · Local mean energy approximation

S.-Y. Jou · C.-T. Hung · Y.-M. Chiu · J.-S. Wu (✉)
Department of Mechanical Engineering, National Chiao Tung University, Hsinchu, Taiwan
e-mail: chongsin@faculty.nctu.edu.tw

B.-Y. Wei
High-Efficiency Gas Discharge Lamps Group, Material and Chemical Research Laboratories, Hsinchu, Taiwan

Introduction

Excimer ultraviolet (EUV) lamps have found wide spreading applications such as surface cleaning, plasma display, LCD backlighting and water quality purification in the past two decades (e.g. [9, 11–13]. However, complicated plasma physics inside the EUV lamp makes the direct measurements of discharge properties either very difficult or impossible. Thus, its design has been mostly depending on the trial-and-error method, which is time-consuming and cost ineffective. Recently, the realistic simulations for gas discharges have become possible due to the rapid advancement of computer technology. Therefore, to understand the plasma physics and chemistry inside a EUV lamp through numerical simulations is helpful and important for the design of better EUV lamps.

The origin of EUV emission is the excimer (originally short for excited dimer) falling from the excited states to the ground state [7]. An excimer is an unstable dimeric. Its lifetime is about 10 ns. The important features of excimer include single wavelength, high efficiency and free radiation direction. Two typical examples are the formation of excimer complexes Xe_2^* and $XeCl^*$, which can emit intensive 172 and 308 nm lines, respectively.

The typical discharge type of a EUV lamp is dielectric barrier discharge (DBD) which is a high-pressure non-equilibrium transient discharge. A primary feature of the dielectric barrier is that it suppresses the occurrence of arc discharges and prevents damage to the metallic electrode through the use of dielectric material. Excimer lamps have first been realized by means of dielectric barrier discharges in xenon gas by [7]. Traditional xenon DBD lamps are generally driven by sinusoidal voltages. The resulting emission efficiency of EUV emission is typically in the range 10–20% and the discharge structure consists of multiple narrow filamentary channels [14]. A dramatic increase in efficiencies up to 60% has been demonstrated experimentally by using short (<750 ns) unipolar voltage pulses interrupted by long idle periods ($\sim$40 μs) [15].

A one-dimensional modeling for xenon DBD using a sinusoidal voltage waveform has been proposed by [10] with gas pressures in the range of 10–400 torr and frequencies in the range of 50 kHz–1 MHz [4] have calculated a VUV generation efficiency as high as 61% using very short voltage pulses [1] have compared the simulation results with experimental values to validate their model. However, it seems that a systematic study for the simulation of a coaxial EUV lamp using pulsed power supply has not been seen in the literature, to the best knowledge of the authors, although it is important from the practical viewpoint.

Thus, the aim of this paper is to simulate a typical coaxial EUV lamp driven by a distorted square power source using one-dimensional fluid modeling method. Effects of several key parameters in designing the EUV lamp, such as the background pressure, driving frequency of the power supply, gap distance and number of dielectric layers, are considered in the simulations.

Remainder of the paper is organized as follows. The fluid modeling is introduced next, which includes the modeling equations, employed plasma chemistry of xenon, numerical method and simulation conditions. Then, the results are presented and discussed where it is necessary. Finally, major findings of the present study are summarized at the end.

Numerical Method

Fluid Modeling Equations

In the framework of fluid modeling, electron and ion number densities are calculated as functions of time and space resulting from the coupled solution of the species continuity equation, species momentum equation, species energy equation, and field equations. Since the fluid modeling equations are similar for most of the gas discharges, we have only summarized a typical set of equations as the model equations for the purpose of demonstration. Note that we have not included flow convection effects in the present study.

The general continuity equation for ion species can be written as,

$$\frac{\partial n_p}{\partial t} + \vec{\nabla} \cdot \vec{\Gamma}_p = \sum_{i=1}^{r_p} S_{p_i} \quad p = 1, \ldots, K \tag{1}$$

where n_p is the number density of ion species p, K the number of ion species, r_p the number of reaction channels that involve the creation and destruction of ion species p, and $\vec{\Gamma}_p$ the particle flux that is expressed, based on the drift-diffusion approximation, as:

$$\vec{\Gamma}_p = sign(q_p)\mu_p n_p \vec{E} - D_p \vec{\nabla} n_p \tag{2}$$

$$\vec{E} = -\nabla \varphi \tag{3}$$

where q_p, $\vec{E}$, μ_p, D_p and α_{iz} are the: ion charge, electric field, electron mobility, electron diffusivity, and ionization rate, respectively. Note that the form of source term S_{p_i} can be modified according to the modeled reactions describing how ion species p is generated or destroyed in reaction channel i. Boundary conditions at the walls have been applied, taking into consideration thermal diffusion, drift and diffusion fluxes.

The continuity equation for electron species e can be written as,

$$\frac{\partial n_e}{\partial t} + \vec{\nabla} \cdot \vec{\Gamma}_e = \sum_{i=1}^{r_e} S_{e_i} \tag{4}$$

where n_e is the number density of ions, r_e the number of reaction channels that involve the creation and destruction of electrons, and $\vec{\Gamma}_e$ the corresponding particle flux that is expressed, based on the drift-diffusion approximation, as:

$$\vec{\Gamma}_e = -\mu_e n_e \vec{E} - D_e \vec{\nabla} n_e \tag{5}$$

where μ_e and D_e are the electron mobility and electron diffusivity, respectively. These two transport coefficients can be readily obtained as a function of electron temperature from the solution of a publicly available computer code for the Boltzmann equation, named BOLSIG+ [2]. As with S_{P_i}, the form of S_{e_i} can also be modified according to the modeled reactions which generate or destroy the ion in reaction channel i. Boundary conditions at the walls are applied, taking into consideration thermal diffusion, drift and the diffusion fluxes of electrons. Secondary electron emissions or photo-electron emissions from the solid walls can be readily added if necessary.

The continuity equation for neutral species can be written as,

$$\frac{\partial n_{uc}}{\partial t} + \vec{\nabla} \cdot \vec{\Gamma}_{uc} = \sum_{i=1}^{r_{uc}} S_{uc_i} \quad uc = 1, \ldots, L \tag{6}$$

where n_{uc} is the number density of uncharged species uc, L the number of neutral species, r_{uc} the number of reaction channels that involve the creation and destruction of uncharged species uc, and $\vec{\Gamma}_{uc}$ the corresponding particle flux, omitting convection effects, which can be expressed as:

$$\vec{\Gamma}_{uc} = -D_{uc}\vec{\nabla}n_{uc} \tag{7}$$

where D_{uc} is the diffusivity of neutral species. Similarly, the form of S_{uc_i} can also be modified according to the modeled reactions which generate or destroy the species in reaction channel i. Neumann boundary conditions at the walls are applied since surface reactions have not been considered in the present study.

The electron energy density equation can be expressed as:

$$\frac{\partial n_\varepsilon}{\partial t} + \nabla \cdot \vec{\Gamma}_{n_\varepsilon} = -e\vec{\Gamma}_e \cdot \vec{E} - \sum_{i=1}^{s_c} \varepsilon_i S_i - 3\frac{m_e}{M} n_e k_B \nu_m \left(T_e - T_g\right) \tag{8}$$

where $n_\varepsilon\left(=\frac{3}{2}n_e k_B T_e\right)$ is the electron energy density, T_e the electron temperature, ε_i the energy loss for the ith inelastic electron collision, k_B the Boltzmann constant, ν_m the momentum exchange collision frequency between electron (mass m_e) and background neutral (mass M), T_g the background gas temperature, and $\vec{\Gamma}_{n_\varepsilon}$ the corresponding electron energy density flux, which can be written as:

$$\vec{\Gamma}_{n_\varepsilon} = \frac{5}{2}k_B T_e \vec{\Gamma}_e - \frac{5}{2}\frac{n_e k_B T_e}{m_e \nu_m}\nabla(k_B T_e) \tag{9}$$

The second term on the right-hand side of Eq. (8) represents the sum of the energy losses of electrons due to inelastic collision with other species. The last term on the right-hand side of Eq. (8) can be ignored for low-pressure gas discharges, although it is important for medium-to-atmospheric pressure discharges. Similarly, boundary conditions at the walls have been applied, taking into consideration thermal diffusion, drift and diffusion fluxes. Secondary electron emission and other boundary effects may be readily added if needed.

Poisson's equation for electrostatic potential can be expressed as:

$$\nabla \cdot (\varepsilon \nabla \varphi) = -\left(\sum_{i=1}^{K} q_i n_i - e n_e\right) \tag{10}$$

where φ is the potential and ε is a function of position, whose value is either the vacuum or dielectric permittivity, depending upon the problem.

Discretization, Numerical Schemes and Algorithms

In the present study, the above equations were recast into a one-dimensional form and discretized using the finite-difference method, which is similar to our previous work [5], except for the addition of the electron energy density equation, which considers the effect of non-local electron transport. The resulting system of nonlinear algebraic equations was then solved using a fully implicit backward Euler's method in the temporal domain, with the Scharfetter-Gummel scheme for mass fluxes in the spatial domain. At each time step, the resulting algebraic nonlinear system was solved by a parallel fully coupled Newton–Krylov–Swartz (NKS) algorithm [3], to solve the nonlinear discretized equations of a large sparse system where an additive Schwarz preconditioned GMRES was used for the solution of the Jacobian system. We have used an inexact or exact solution, such as

incomplete LU (ILU) or LU factorizations, in each subdomain for the preconditioning. We evaluated the Jacobian matrix entries using a hybrid analytical-numerical method, in which the entries involving the derivative, with respect to number density (e.g. the source terms of species continuity equations), could be easily expressed analytically without resorting to numerical approximation. Other entries were evaluated using a standard finite-difference method. This strategy was especially useful for plasma simulations with a large number of species and reaction channels. Details of this implementation have been presented elsewhere [6] and are skipped here for brevity.

Transport and Rate Coefficients for Electrons and Ions

Electron energy distribution functions (EEDFs) were calculated by solving the stationary spatially homogeneneous Boltzmann equation using BOLSIG [2], complemented with more recent electron collision section data. Electron collision rate coefficients and transport coefficients, calculated from cross-section data and the EEDFs, depend directly on the mean electron energy (local mean energy approximation, LMEA) rather than on the reduced electric field, known as the local field approximation (LFA). This was especially important in the present study since the electron temperature distribution was not uniform at all, as will be seen in a later section. This allowed us to model electron-induced kinetics more rigorously, which has been shown previously [8].

Discharge Current, Dielectric Voltage and Gap Voltage

The discharge current $i_T(t)$ is the sum of the conduction current $i_C(t)$ and the displacement current $i_D(t)$:

$$i_T(t) = i_C(t) + i_D(t) \tag{11}$$

The voltage between the electrodes $V_s(t)$ is given as:

$$V_s(t) = V_d(t) + V_g(t) \tag{12}$$

where $V_d(t)$ is the dielectric voltage and $V_g(t)$ is the gap voltage.

VUV Emission Efficiency

Since we only considered one-dimensional radial fluid modeling, the input power density, P_{in} (or dissipated power), to the discharge is thus defined as:

$$P_{in} = \frac{2}{T(r_2^2 - r_1^2)} \int_0^T \int_{r_1}^{r_2} j_c(r,t) E(r,t) r dr dt \tag{13}$$

where T is the period of the applied voltage and j_c is the conduction current density caused by the electrons and ions. Note that r_1 and r_2 are the inner and outer radii of the gas gap, and are fixed as 0.8 and 1.25 cm, respectively, in the current study. The VUV (vacuum UV) light output power density, $P_{out,k}$, generated from the kth kind of excited species, is defined as:

$$P_{out,k} = \frac{2h\nu_k}{T(r_2^2 - r_1^2)} \int_0^T \int_{r_1}^{r_2} \frac{n_k(r,t)}{\tau_k} r dr dt \tag{14}$$

where hv_k, τ_k and n_k are the photon energy of the VUV light, lifetime and concentration of the excimer species, respectively. Thus, the VUV emission efficiency due to kth excimer species is given as:

$$\eta_k = \frac{P_{out,k}}{P_{in}}. \tag{15}$$

Xenon Plasma Chemistry

In the current study, we have used the simplified xenon plasma chemistry that is the same as that used in [10], which consists of 9 species and 24 reaction channels, as listed in Table 1. These reaction channels included electron-neutral elastic collision (No. 1 in Table 1), direct electron impact ionization (No. 2 in Table 1), excitation (No. 3–5 in Table 1), stepwise ionization (No. 6 in Table 1), recombination (No. 7 in Table 1), heavy particle collisions (No. 8–18 in Table 1) and radiation processes among electrons, ions, associated excited atoms, excimer xenon and ground-state xenon atoms (No. 19–24 in Table 1).

Results and Discussion

Typiin Cal Discharge Physics and Chemistry

In order to describe the behavior of power deposition and emission, we should understand the discharge physics and chemistry inside the xenon lamp driven by the realistic bipolar square voltages in detail. We first describe the overview of the discharge using the phase diagrams of several key discharge properties next, followed by the details of the discharge in each period by the following simulation conditions.

Simulation Conditions

Figure 1 depicts a sketch of the coaxial xenon excimer lamp simulated in the present study. The distorted bipolar square voltage waveform used in the simulation is also shown at the top left side, which is a typical one used for sustaining the xenon discharge. We term this as "distorted" bipolar square because it is not a standard bipolar square one. The peak value of pulse is 3.2 kV. For explaining the typical discharge physics and chemistry, we have selected the following simulation conditions for convenience. The tube length was 70 cm, the gap distance (d) in the radial direction was 3 mm, and both the inner and outer quartz tubes ($d_i + d_o$) were 1 mm thick. An inner-powered electrode with a radius of 7 mm, was placed in direct contact with the inner quartz tube and an outer mesh grounded electrode ($\sim$92% in porosity) with a radius of 12 mm, was placed outside the outer quartz tube. The complicated three-dimensional geometrical structure was simplified as a one-dimensional radial coordinate system in the current study, as the first step in understanding the discharge physics and chemistry without the complications of geometry. The dielectric constant of the quartz tube was 4.0, and power supply frequency f and xenon gas pressure p were fixed at 50 kHz and 400 torr, respectively.

Table 1 The reaction channels of the simplified xenon discharge [10]

No	Reaction	ε_e(eV)	Reaction rate
Momentum transfer			
1	$e^- + Xe \rightarrow Xe + e^-$	0.0	Bolsig [2]
Impact ionization			
2	$e^- + Xe \rightarrow Xe^+ + 2e^-$	12.1	Bolsig [2]
Excitation			
3	$e^- + Xe \rightarrow Xe^*(ex) + e^-$	9.57	Bolsig [2]
4	$e^- + Xe \rightarrow Xe^*(res) + e^-$	8.44	Bolsig [2]
5	$e^- + Xe \rightarrow Xe^*(met) + e^-$	8.32	Bolsig [2]
Stepwise ionization			
6	$e^- + Xe^*(met) \rightarrow Xe^+ + 2e^-$	3.44	Bolsig [2]
Recombination			
7	$e^- + Xe_2^+ \rightarrow Xe^*(ex) + Xe$	11.1	$2.0 \times 10^{-7} T_e^{-0.5}$ cm^{3}s^{-1} [10]
Conversion to excited state			
8	$Xe^*(ex) + Xe \rightarrow Xe^*(res) + Xe$	0.0	2.0×10^{-11} cm^{3}s^{-1} [10]
9	$Xe^*(ex) + Xe \rightarrow Xe^*(met) + Xe$	0.0	2.0×10^{-11} cm^{3}s^{-1} [10]
10	$Xe^*(res) + Xe \rightarrow Xe^*(met) + Xe$	0.0	2.2×10^{-14} cm^{3}s^{-1} [10]
11	$Xe^*(met) + Xe \rightarrow Xe^*(res) + Xe$	0.0	1.5×10^{-15} cm^{3}s^{-1} [10]
Conversion to dimmers			
12	$Xe^*(res) + 2Xe \rightarrow Xe_2^*(O_u^+) + Xe$	0.0	1.55×10^{-31} cm^{6}s^{-1} [10]
13	$Xe^*(met) + 2Xe \rightarrow Xe_2^*(^3\Sigma_u^+) + Xe$	0.0	8.53×10^{-32} cm^{6}s^{-1} [10]
14	$Xe_2^*(O_u^+) + Xe \rightarrow Xe_2^*(^1\Sigma_u^+) + Xe$	0.0	8.7×10^{-11} cm^{3}s^{-1} [10]
Excited -excited collision induced ionization			
15	$Xe^*(res) + Xe^*(res) \rightarrow Xe^+ + Xe + e^-$	0.0	5.0×10^{-10} cm^{3}s^{-1} [10]
16	$Xe^*(met) + Xe^*(met) \rightarrow Xe^+ + Xe + e^-$	0.0	5.0×10^{-10} cm^{3}s^{-1} [10]
17	$Xe^*(res) + Xe^*(met) \rightarrow Xe^+ + Xe + e^-$	0.0	5.0×10^{-10} cm^{3}s^{-1} [10]
Ion conversion (three-body collision)			
18	$Xe^+ + Xe + Xe \rightarrow Xe_2^+ + Xe$	0.0	8.0×10^{-32} cm^{6}s^{-1} [10]
VUV emission			
19	$Xe_2^*(^1\Sigma_u^+) \rightarrow 2Xe + h\nu$ (172nm)	0.0	1.82×10^8 s^{-1} [10]
20	$Xe_2^*(^3\Sigma_u^+) \rightarrow 2Xe + h\nu$ (172nm)	0.0	1.0×10^7 s^{-1} [10]
21	$Xe_2^*(O_u^+) \rightarrow 2Xe + h\nu$ (152nm)	0.0	9.0×10^6 s^{-1} [10]
22	$Xe^*(res) \rightarrow Xe + h\nu$ (147nm)	0.0	4.3×10^5 s^{-1} [10]
Radiation to lower level (visible and infrared)			
23	$Xe^*(ex) \rightarrow Xe^*(res) + h\nu'$	0.0	2.7×10^7 s^{-1} [10]
24	$Xe^*(ex) \rightarrow Xe^*(res) + h\nu''$	0.0	2.53×10^7 s^{-1} [10]

Phase Diagrams of Key Discharge Properties

Figure 2 shows the spatiotemporal diagrams of the concentrations of the charged species (electron, Xe^+ and Xe_2^+), while Fig. 3 shows the same diagrams of Xe^*(met) and $Xe_2^*(^3\Sigma_u^+)$ (two important excited species for VUV 172 nm emission) together with electron temperature. Note that we have only shown $Xe_2^*(^3\Sigma_u^+)$, instead of $Xe_2^*(^1\Sigma_u^+)$, because the

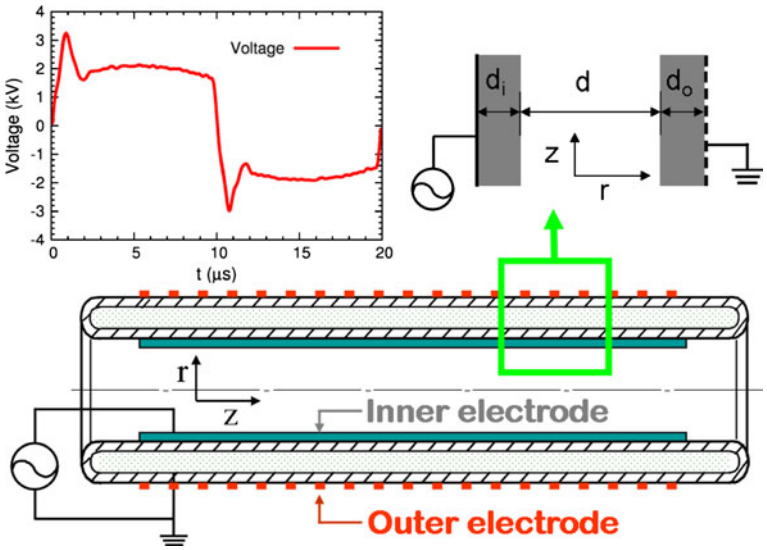

Fig. 1 Schematic diagram of the coaxial DBD lamp and the applied distorted bipolar square voltage waveform (50 kHz)

concentration of the former is found to be much greater than the latter. We divide these phase diagrams into six periods in the temporal direction according to the temporal variation of electron number density, as only electrons can respond immediately to variations of the electric field. Periods I and IV are pre-discharge regions, Periods II and V are discharge regions, and Periods III and VI are post-discharge regions. Periods II and V are further divided into two sub-periods (II-1 and II-2; V-1 and V-2). The trends of gas discharge properties in the second half cycles (IV, V and VI) are very similar to those of the first half cycles (I, II and III), except that there are some slight differences in the properties because of the different areas of the inner and outer electrodes. Note that the blue dashed and black solid curves in the top of Fig. 2 represent the temporal variation of the spatial-averaged number density of electrons in the gap and applied voltages, respectively. For brevity, we only describe the discharge physics and chemistry in the first half cycles (I, II and III) in detail next, as those in the second half cycles are fundamentally the same, with the exception as mentioned in the above.

Period I In this pre-discharge period, the spatially averaged number density of electrons decreases slightly with time because the electrons are attracted to the anode side (inner electrode) and accumulated on the inner dielectric tube surface due to its rising voltage. In the earlier part of Period I (negative applied voltage, 19.57–20 μs in both Figs. 2, 3), the concentrations of all species are low, especially the excited and meatastable xenon, because the electron energy is still quite low.

In the later part of Period I (positive applied voltage, 0–0.25 μs in both Figs. 2, 3), in the central region of the gap ($r \approx 0.9$–1 cm), the concentration of the atomic xenon ions (Xe^+) increases up to $\sim 10^6$ (cm^{-3}), as a result of direct impact ionization, as shown in the middle of Fig. 2. Although the electron temperatures are very high near the outer dielectric tube (cathode side) (see bottom of Fig. 3) due to the rising voltage at the inner electrode, breakdown does not occur because of the very small number of electrons existing in that

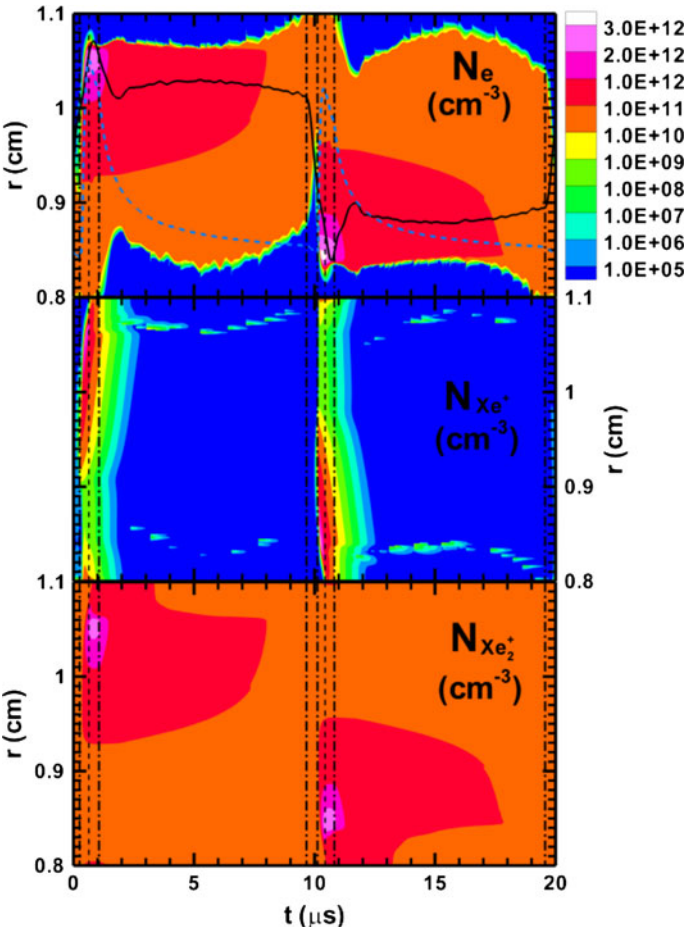

Fig. 2 Spatiotemporal diagram of number densities of charged species: electron (*upper*), atomic xenon ion (*middle*) and molecular xenon ion (*bottom*)

region (see top of Fig. 2). At the same time, both the concentrations of Xe^*(met) and $Xe_2^*(^3\Sigma_u^+)$ increase to the order of $\sim 3 \times 10^9$ (cm^{-3}) in the central region of the gap. In addition, molecular xenon ions (Xe_2^+) become abundant ($>7 \times 10^{10}$ cm^{-3}) throughout the complete period; this result is due to the ion conversion, i.e., three-body collision (No. 18 in Table 1). Near the inner dielectric tube ($r \approx 0.81$–0.9 cm), the quasi-neutrality is held with a plasma density of $\sim 7 \times 10^{10}$ cm^{-3} ($n_e \approx n_{Xe_2^+} \gg n_{Xe^+}$), while the molecular xenon ions (Xe_2^+) prevail across the gap. At the end of Period I, the electric field near the outer dielectric tube is gradually enhanced by the "cathode-directed streamer-like" ionization wave at which point the breakdown occurs instantaneously at the start of Period II.

Period II This discharge period is further divided into two sub-periods, II-1 and II-2. In Period II-1, the breakdown occurs at $r \approx 0.9$ cm, where the number of electrons increases dramatically (see top of Fig. 2), and the electrons move towards the outer quartz tube at a speed of $\sim$4,000 m/s (from anode towards cathode) by direct electron impact ionization.

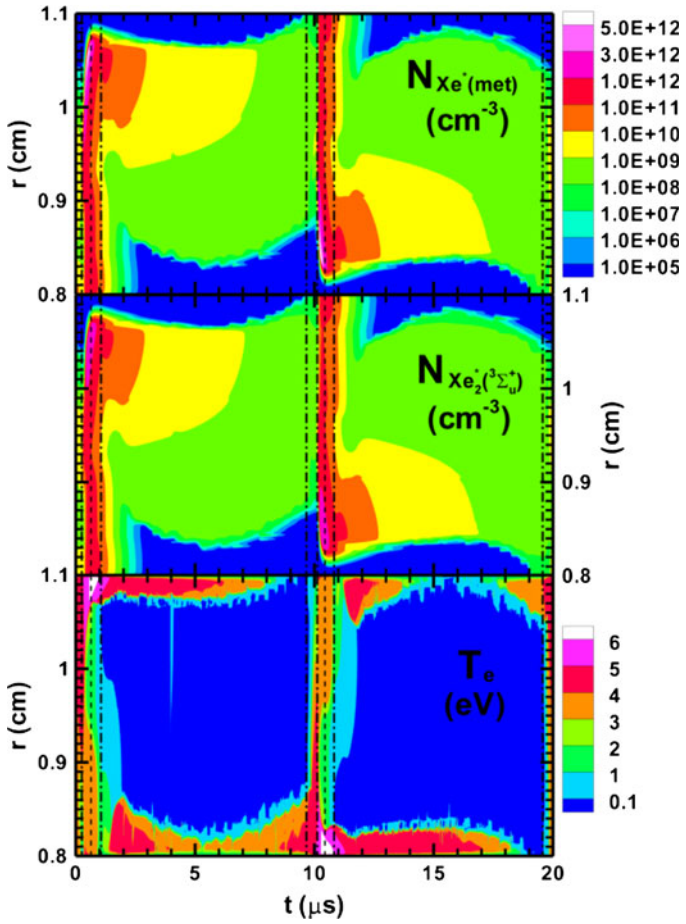

Fig. 3 Spatiotemporal diagram of number densities of excited species: Xe^*(met) (*upper*), $Xe_2^*(^3\Sigma_u^+)$ (*middle*) and electron temperature (*bottom*)

We term this as "cathode-directed streamer-like" ionization wave. The number of electrons rapidly increases to the maximal value ($>2.78 \times 10^{12}$ cm^{-3}) within $\sim$0.388 μs at $r \approx 1.06$ cm, and then decreases gradually afterwards (see top of Fig. 2). At the same time, the number of molecular xenon ions increases rapidly in the same fashion through the three-body collision channel (No. 18 in Table 1), which indeed quickly consumes the atomic xenon ions. The molecular xenon ion thus becomes the most dominating ion species in Period II-2 (see bottom of Fig. 2). In addition, both Xe^*(met) and $Xe_2^*(^3\Sigma_u^+)$ are also abundant across the gap because of the excitation of ground-state xenon by the still energetic electrons: $T_e > 3$ eV (No. 3 and No. 5 in Table 1; see top and middle of Fig. 3). Interestingly, the temporal location where the maximal amount of $Xe_2^*(^3\Sigma_u^+)$ occurs is shifted slightly after that of the maximal amount of Xe^*(met) because the former is formed solely through the conversion-to-dimer reaction between Xe^*(met) and ground-state xenon (No. 13 in Table 1).

In Period II-2, which lasts less than 4.2 μs, the quasi-neutral region is formed across the gap with a very high plasma density (>2 × 10^{12} cm^{-3}) between the $r \approx 1.04$–1.06 cm, and move slowly from the cathode side (outer grounded) to the anode side (inner powered). Xe_2^+ becomes the most dominating ion species formed through the three-body collision as described earlier. In addition, both Xe^*(met) and $Xe_2^*(^3\Sigma_u^+)$ begin to disappear because of the conversion-to-dimer reaction (No. 13 in Table 1) and intense photon emission (172 nm, No. 20 in Table 1) occurs in Period II-2. In the region of $r \approx 0.93$–1.07 cm, having begun in Period II-1, the electron temperature decreases rapidly with time because of the energy loss by ionization and excitation of the ground-state xenon.

Period III In this post-discharge period, the quasi-neutral region expands slowly from the cathode side (outer) towards the anode side (inner) with the temporally decreasing plasma density in the bulk and plasma sheath near both dielectric surfaces (see top and bottom of Fig. 2). This is attributed to the discharge quenched through a vanishing electric field across the gap (nearly zero) by the shielding effect, although the applied voltage is still as high as 2 kV in this post-discharge period. In the latter part of Period III, the electrons begin to move away from the anode side (inner) towards the cathode side (outer) at $t = 5$–6 μs, when the applied voltage decreases from the peak (see top of Fig. 2). In Period III, both Xe^*(met) and $Xe_2^*(^3\Sigma_u^+)$ decreases to a very small amount (< 10^9 cm^{-3}), except in the early part near the cathode (outer), because the electron temperatures are very low, down to even 0.1 eV in most of the region in Period III.

Typical Characteristics of Power Deposition and VUV Emission

Figure 4 shows the cycle averaged data of VUV emission (upper figure) and power deposition of charged species (bottom figure) across the discharge gap over a cycle. It can be found that 172 nm line of VUV is the major source of VUV emission as compared to the other two lines (147 and 152 nm). It can also be noted that the strength of VUV power emission in the inner side is larger than that in the outer side because the electric field in the inner side is stronger than in the outer side. In the bottom figure, it can be found that electron power deposition occurs mainly across the discharge gap and ion power deposition occurs mainly in the sheath region. In addition, the amount of ion power deposition density in the inner side is nearly 1.67 times than in the outer side. The reason is the same as the variation of VUV power emission because of larger electric field in the inner side with the characteristic due to smaller radius of curvature. The trend of 172 nm line of VUV power emission (top) is similar to that of electron power emission (bottom) because, through the collision of energetic electrons, more species Xe^*(met) and $Xe_2^*(^3\Sigma_u^+)$ are generated, leading to 172 nm radiation.

Figure 5 shows the phase diagrams of VUV power emission ($\lambda = 172$ nm) (upper figure) and electron power deposition (bottom figure) over a cycle, while Fig. 6 shows the phase diagrams of ion power deposition (Xe^+ in the upper and Xe_2^+ in the bottom figure). Again, we only describe the variations of power deposition and VUV radiation in the first half cycle (I, II and III) in detail. Besides, the slightly difference of the amount of the above properties results from the different areas of the inner and outer electrodes.

Period I In the earlier part of Period I (negative applied voltage, 19.57–20 μs in both Figs. 5, 6), it can be found that electrons responded to the variations of electric field immediately, which leads to increasing electron power deposition in the region of $r = 0.9$–1.0 cm. Accordingly, the concentrations of metastable and excimer species start to increase in the

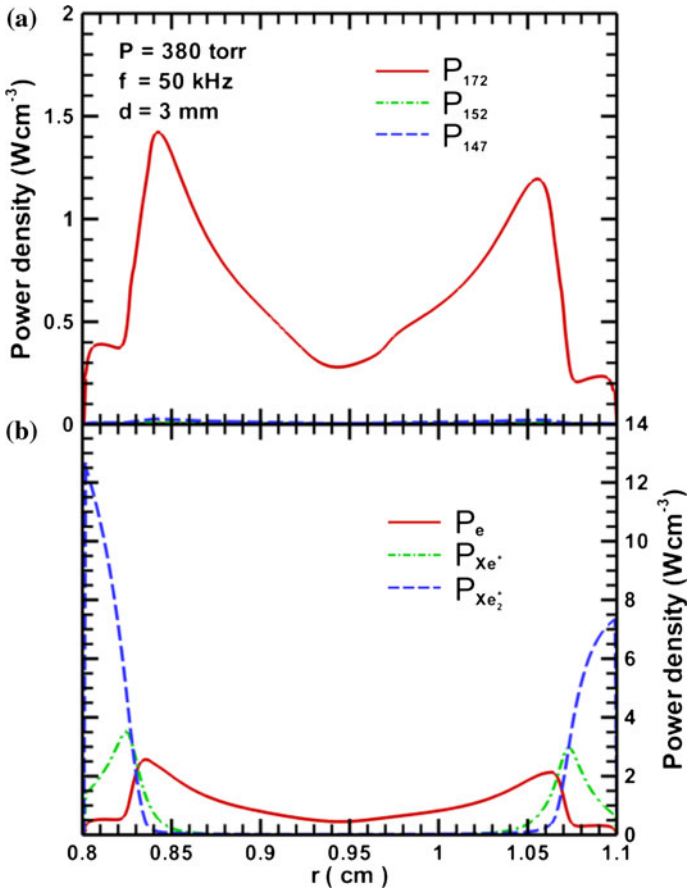

Fig. 4 Spatial distribution of cycle averaged discharge properties: **a** VUV light emissions across the gap **b** power depositions of charged species across the gap

region of $r = 0.9$–1.0 cm (see top and middle of Fig. 3) due to electron impact collisions. Thus, power emission of 172 nm line also increases with the increasing of concentrations of metastable and excimer species. Generally, power deposition of Xe^+ is less than the order of 10^{-2} (Wcm^{-3}) although number density of Xe^+ increases up to 10^5 (cm^{-3}) (see Fig. 2). At the same time, power deposition of Xe_2^+ mainly occurs in the outer sheath region.

In the later part of Period I (positive applied voltage, 0–0.25 μs in both Figs. 5, 6), energetic electrons, moving from the outer sheath into the bulk ($r \approx 0.9$–1.0 cm), generates many excited species such as Xe^*(met) and $Xe_2^*(^3\Sigma_u^+)$ in the bulk (see Fig. 3). VUV emission thus rises to the order of 1 (Wcm^{-3}). The concentration of Xe^+ increases up to $\sim 10^6$ (cm^{-3}), as a result of direct impact ionization, as shown in the middle of Fig. 2. However, the power deposition of Xe^+ is still less than the order of 10^{-2} (Wcm^{-3}) because the number density of Xe^+ is too small in this period (see middle of Fig. 2). In contrast, the power deposition of Xe_2^+ is much higher than the order of 1 (Wcm^{-3}) because very large amount of Xe_2^+ exists in this region and large electric field in the outer sheath. Near the outer dielectric tube (cathode side), although the electric field is very high due to the rising voltage at the inner electrode, both VUV power emission and electron power deposition are

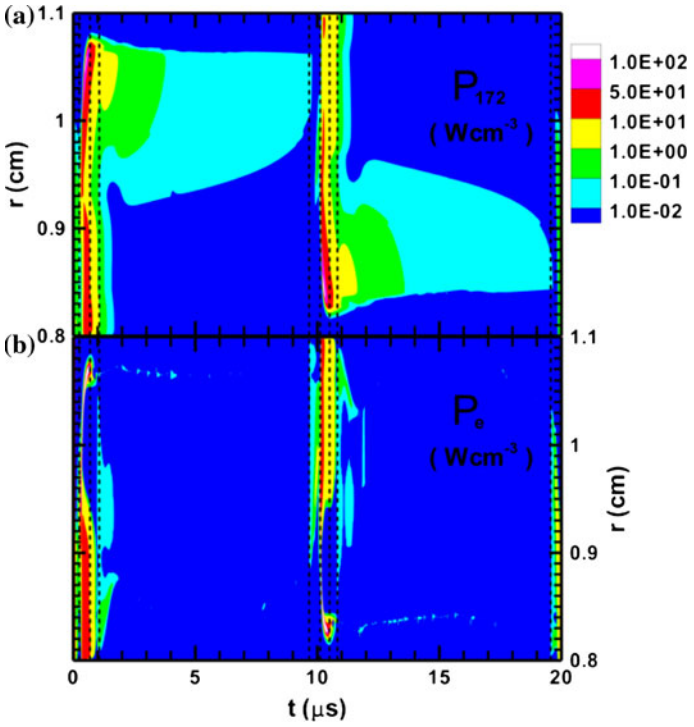

Fig. 5 Spatiotemporal diagram of: **a** 172 nm *line* UVU light emission and **b** electron power deposition

weak because of very few Xe^*(met), $Xe_2^*(^3\Sigma_u^+)$ and electrons (see Figs. 2, 3) in this region. Thus, it can be observed that the major power deposition of Xe_2^+ is in the region of $r \approx 0.92$–1.1 cm in the sheath where a large potential drop exists.

Period II In Period II-1, electron power deposition increases dramatically and the peak moves towards outer quartz tube in a speed of ~4,000 m/s (from anode towards cathode, see bottom of Fig. 5) due to the huge growth of electron number density by direct electron impact ionization (see top of Fig. 2). The amount of electron power deposition rapidly increases to the maximal value ($>1 \times 10^3$ Wcm^{-3}) within ~0.388 μs at $r \approx 1.06$ cm and then decreases gradually afterwards (see bottom of Fig. 5). The moving direction of Xe^+ power deposition is the same as the electrons, with the maximal value of 7×10^2 (Wcm^{-3}) located at $r \approx 1.06$ cm, which is smaller than that of the electrons due to its heavier mass. Afterwards, the power deposition Xe^+ decreases gradually in Period II-2 (see top of Fig. 6). At the same time, number of Xe_2^+ increases through the three-body ion conversion channel (No. 18 in Table 1), and thus Xe_2^+ power deposition increases towards the cathode (see bottom of Fig. 6). However, the power deposition of Xe_2^+ is smaller than that of Xe^+ because the former is about two times heavier than the latter. In addition, both Xe^*(met) and $Xe_2^*(^3\Sigma_u^+)$ are both highly abundant across the gap (see Fig. 3) because of the excitation of ground-state xenon (No. 3 and 5 in Table 1) by the collision of energetic electrons. During this period, the 172 nm VUV power emission (see top of Fig. 5) originates from the process that both the excimer species $Xe_2^*(^1\Sigma_u^+)$ (less dominating) and $Xe_2^*(^3\Sigma_u^+)$ (most dominating) fall to the ground state (No. 19 and 20 in Table 1).

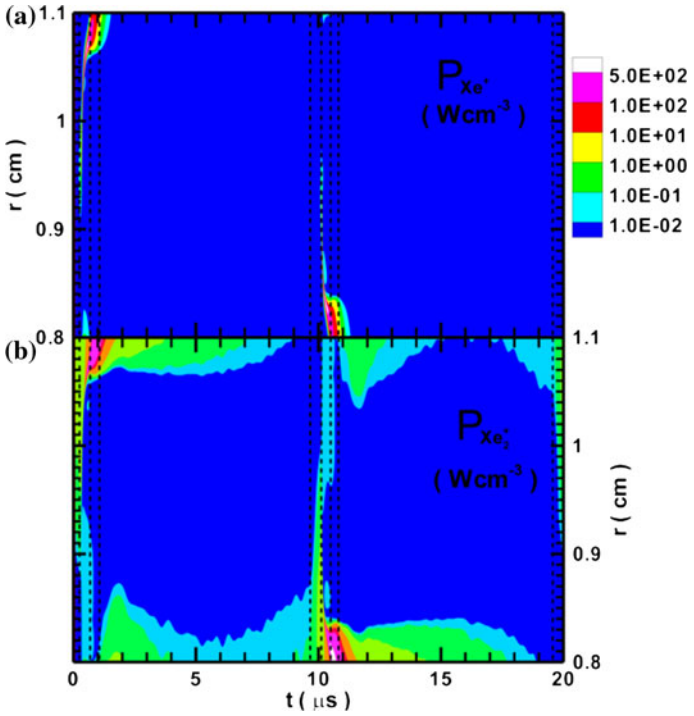

Fig. 6 Spatiotemporal diagram of power depositions: **a** atomic xenon ion and **b** molecular xenon ion

In Period II-2, both Xe^*(met) and $Xe_2^*(^3\Sigma_u^+)$ begin to disappear because of less energetic electrons existing in the bulk region ($r \approx 0.75$–1.30 cm; see bottom of Fig. 3), which in turn reduces the VUV emission (P_{172}) dramatically (see top of Fig. 5). In the cathode sheath region, highly depleted electrons (see top of Fig. 2) can not absorb enough energy from the electric field which leads to much less power deposition of electrons (bottom of Fig. 5). At the same time, Xe^+ is rapidly consumed by Xe_2^+ through the three-body collision as described earlier. Thus, the power deposition of Xe_2^+ is much larger than that of Xe^+ as can be clearly seen in the cathode sheath (Fig. 6). Noticeably, the maximal value of Xe_2^+ power deposition can reach a value of 4×10^2 (Wcm^{-3}) in the cathode sheath region.

Period III In this post-discharge period, the VUV emission decays with time in the bulk region, which strongly correlates with the variation of number densities of both Xe^*(met) and $Xe_2^*(^3\Sigma_u^+)$, as shown in Fig. 3 and top of Fig. 5. In addition, power deposition to charged particles mainly goes through the Xe_2^+ remaining in the cathode sheath throughout Period III (see bottom of Fig. 6). Note the power deposition in the bulk region with much more Xe_2^+ is much smaller as compared to that in the cathode sheath mainly because of much smaller electric field in this region.

General VUV Emission Power and Efficiency

Four parameters, which include driving frequency of the power source, background gas pressure, gap distance between electrodes and number of dielectric layers, are varied

Table 2 Test conditions for the parametric study

Frequency (f) (P:400 torr, d:4.5 mm, Nd: 2)	Pressure (P) (f :50 kHz, d:4.5 mm, Nd: 2)	Gap distance (d) (P:400 torr, f :50 kHz, Nd: 2)	Num. of dielectric (Nd) (P:400 torr, f:50 kHz, d:4.5 mm)
Test parameters			
10–100 (kHz)	100–700 (torr)	0.5–5 (mm)	One-dielectric & Two-dielectric

Dielectric thickness: 1 (mm)

Permittivity of dielectric material: 4 (F/m)

systematically to study their effects on the efficiency of 172 nm line (η_{172}), the total power deposition (P_{tot}) and the VUV emission from 172 line (P_{172}). The test conditions are summarized in Table 2.

Effect of Frequency Variation

Figure 7a shows that η_{172}, P_{tot} and P_{172} all increase with increasing frequency in the range of 10–100 kHz under the condition of 400 torr (pressure), 4.5 mm (gap distance) and 2 dielectric layers. Interestingly, the efficiency η_{172} increases only slightly from 24.4% (10 kHz) to 31.4% (100 kHz), while total emission power increased dramatically from 102.9 W (10 kHz) to 781.4 W (100 kHz). Corresponding total absorption powers are plotted in Fig. 7b, which shows that the energy absorbed by the electrons increases almost 10 times with 10 times of frequency increase (37–370 W vs. 10 to 100 kHz), while the energy absorbed by the ions (especially the Xe_2^+) began to level off with increasing frequency. This means that only the very light electrons could efficiently absorb the energy from the oscillating electric field, while the much heavier ions could not because of very large inertia. Albeit the P_{Xe^+} (11.9 (W) to 182.1 (W)) and the $P_{Xe_2^+}$ (52.9 (W) to 213.1 (W)) increased with increasing frequency (10–100 kHz), the fraction of P_{Xe^+} (11.6–23.3%) increases and $P_{Xe_2^+}$ (51.2–29.57%) decreases with increasing frequency, as shown in Fig. 7c. In addition, the slight increase of VUV emission efficiency (Fig. 7a) with increasing frequency is attributed to the increasing fraction of power deposition through the electrons as compared to the heavy Xe_2^+ (Fig. 7c), in which the electrons are able to excite more VUV emission species such as Xe^*(met) and $Xe_2^*(^3\Sigma_u^+)$.

In Fig. 7b, c, they show that most of the energy is absorbed by the heavier Xe_2^+, while only a smaller fraction is absorbed by the electrons and even much smaller fraction by the Xe^+ at lower frequencies (<50 kHz). In contrast, most of the energy is absorbed by the electrons at higher frequencies (>50 kHz), while the fraction of energy absorbed by the Xe_2^+ becomes much smaller. In addition, we can find that the fraction of energy absorbed by the electrons over a cycle increases slightly (37–47%) with increasing frequency, but that of the heavier ions (Xe_2^+) decreases quickly (52–30%) with increasing frequency. The larger the value of $|dV/dt|$ is (at higher frequency), the easier the electrons as compared to other ions could absorb energy per unit time since only they could respond instantly (almost without inertia) to gain energy from the oscillating electric field efficiently without much elastic and inelastic collision loss (No. 7 in Table 1).

Based on the above observation, we can simply conclude that more power deposited through the electrons benefits the absolute VUV emission power and corresponding efficiency.

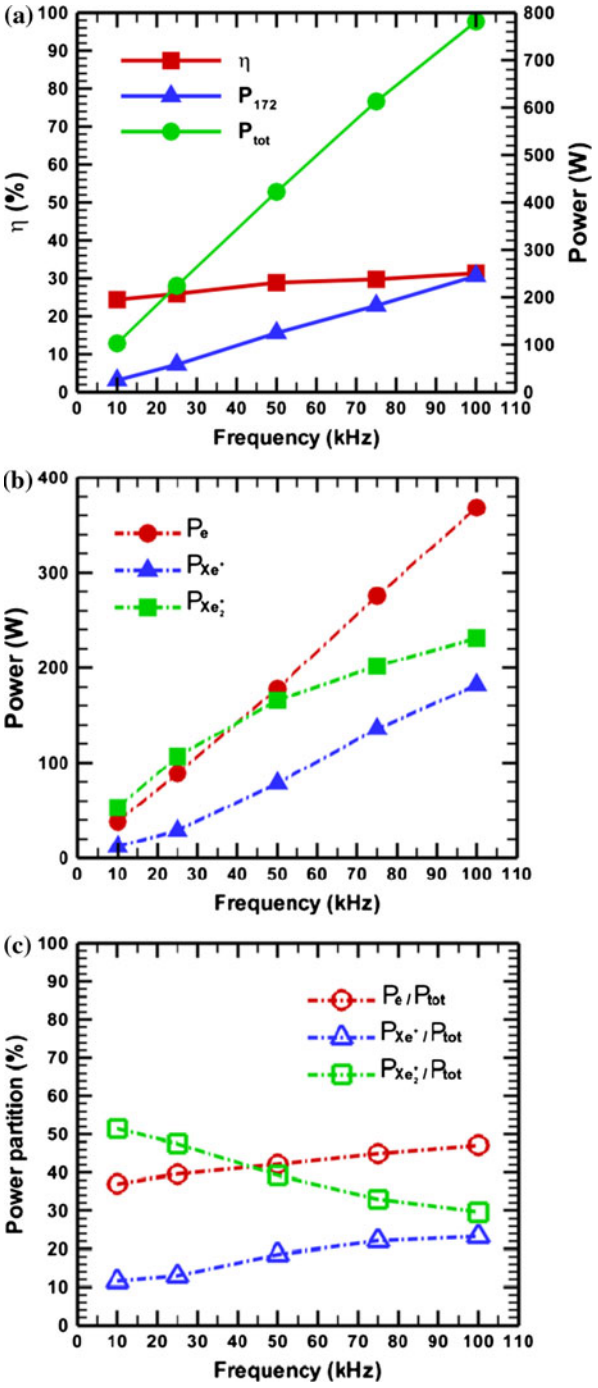

Fig. 7 Effect of frequency on: **a** P_{tot} and P_{172}, **b** power deposition of various charged species, and **c** fraction of power deposition for different charged species at 400 torr of gas pressure, 4.5 mm of gap distance and 2 dielectric layers

Effect of Background Gas Pressure Variation

Figure 8a shows that η_{172}, P_{172} and P_{tot} at various gas pressures under the condition of 50 kHz (frequency), 4.5 mm (gap distance) and 2 dielectric layers. Results show that η_{172} increases from 7.9 to 39.4% as background gas pressure increases from 100 to 700 torr, while both P_{172} and P_{tot} have peak values of 320 W and 475 W, respectively, at 600 torr. Reason causing this observation will be explained later. Figure 8b shows the partition of power deposition through different types of charged species at various gas pressures. Fraction of the power deposition for different charged species changes at different pressures, which can be also seen from Fig. 8c (ratios of absorbed to total power for different charged species). Results show that power absorbed through the electrons increases with almost linearly with increasing pressure, but reaches a peak value of $\sim$260 W at a pressure of 600 torr. Furthermore, power absorbed through the Xe_2^+ increases with gas pressure, but levels off very soon at $\sim$160 W at pressures of 300–400 torr. In addition, power absorbed through Xe^+ decreases with increasing gas pressure and monotonically reaches a value as low as $\sim$25 W at 700 torr. This is attributed to more intense three-body ion conversion reaction (No. 18 in Table 1) at higher pressures. Equivalently, at lower pressures, power is mostly absorbed through the Xe^+ in the cathode sheath, at which the very few Xe_2^+ exists. At higher pressures, the power deposition through the electrons becomes the dominant process, while that through Xe^+ becomes less important because most of them disappear through the intense three-body ion conversion reaction as mentioned earlier.

Figures 9a, b show the cycle averaged power distribution in the discharge space for electrons, Xe^+ and Xe_2^+, respectively. Figure 9a (very similar to the P_e curve in the bottom of Fig. 4) shows that P_e generally increases everywhere in the gap with increasing pressure, except near the pressures of 600–700 torr, as similarly shown in Fig. 8b. The reason should be attributed to the increasingly frequent elastic collision loss near the pressures of 600–700 torr. On the contrary, Fig. 9b shows that P_{Xe^+} in the sheaths generally decreases with increasing pressure monotonically, as similarly shown in Fig. 8b. However, Fig. 9c shows that $P_{Xe_2^+}$ in the both sheaths increase with increasing pressure first (prior to 300–400 torr) and then become essentially the same or even decrease slightly afterwards. The latter is attributed to the smaller speed of the Xe_2^+ when accelerating in the sheaths due to increasing background gas pressure, although the Xe_2^+ becomes more abundant.

Effect of Gap Distance Variation

Figure 10a shows that η_{172}, P_{tot} and P_{172} are plotted as a function of gap distance under the condition of 50 kHz (frequency), 400 torr (pressure) and 2 dielectric layers. Results show that η_{172} increases from 6 to 30% as the gap distance increases from 0.5 to 5 mm. Figure 10b shows the partition of power deposition through different types of charged species at various gap distances. Fractions of the power deposition for different charged species change at different gap distances, which can be also seen from Fig. 10c (ratios of absorbed to total power for different charged species). Results show that power absorbed through the electrons increases with increasing gap distance and can reach a value of $\sim$240 W at $d = 5$ mm. Furthermore, power absorbed through the Xe_2^+ increases with gas distance rapidly initially ($d \leq 1$ mm), but reaches a peak value of $\sim$175 W between $d = 2$ and 3 mm and then decreases slightly with increasing gap distance. In addition, power absorbed through Xe^+ increased slightly with increasing gas pressure monotonically reaching a value of $\sim$75 W at $d = 5$ mm. In brief summary (see Fig. 10c), the larger the

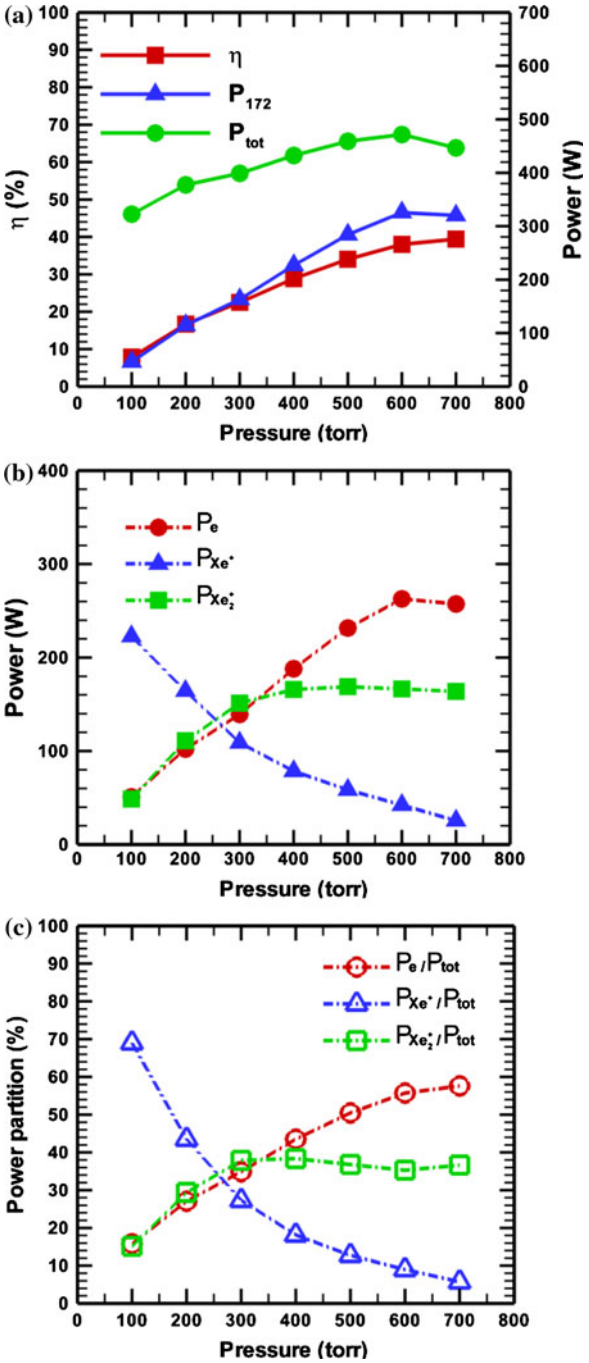

Fig. 8 Effect of gas pressure on: **a** P_{tot} and P_{172}, **b** power deposition of various charged species, and **c** fraction of power deposition for different charged species at 50 kHz of power source, 4.5 mm of gap distance and 2 dielectric layers

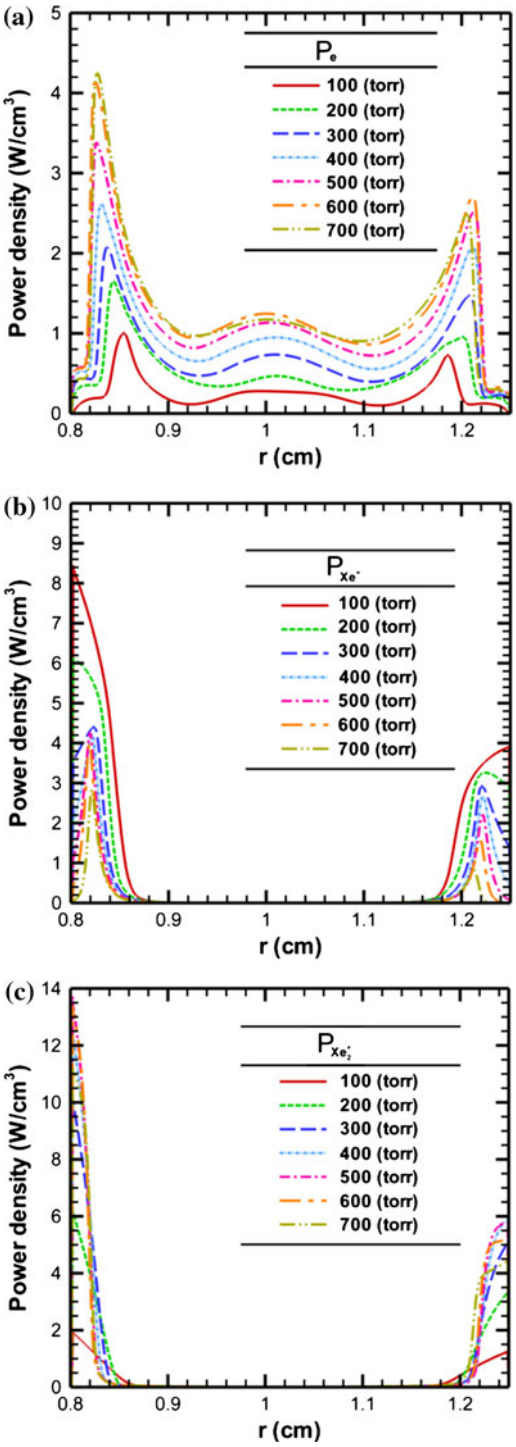

Fig. 9 Spatial distribution of cycle-averaged power densities of various charged species at different gas pressus: **a** electron, **b** atomic xenon ion and **c** molecular xenon ion

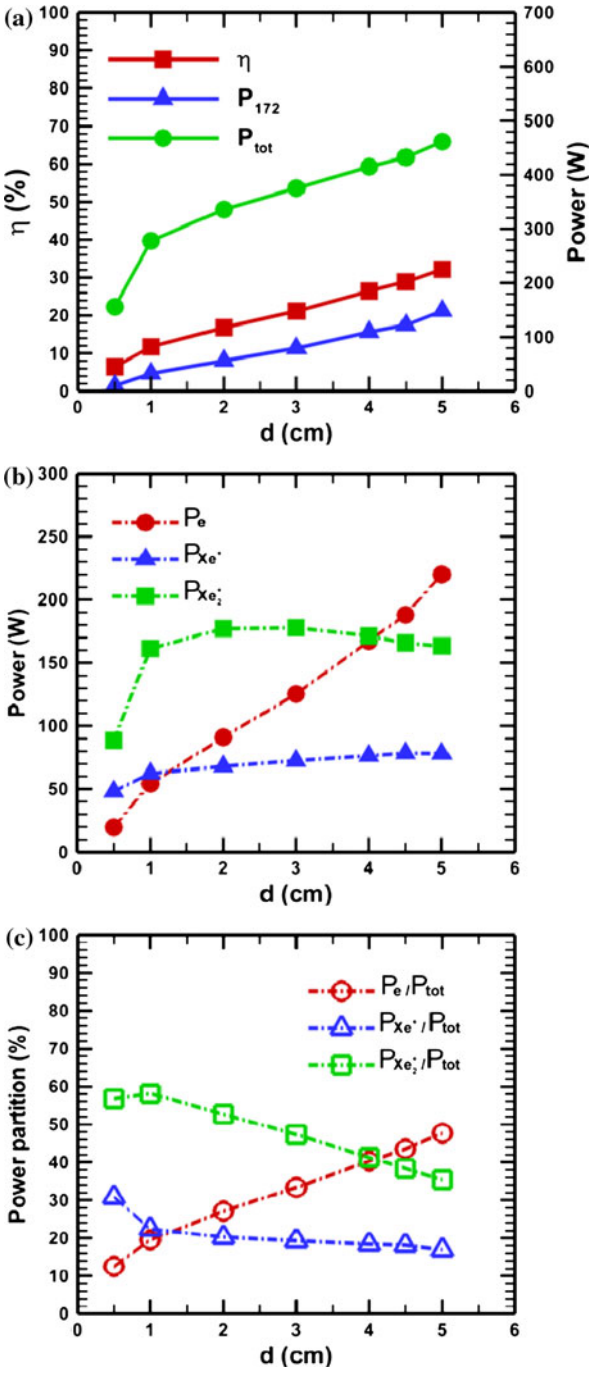

Fig. 10 Effect of gap distance on: **a** P_{tot} and P_{172}, **b** power deposition of various charged species, and **c** fraction of power deposition for different charged species at 50 kHz of power source, 400 torr of gas pressure and 2 dielectric layers

gap distance is the larger the fraction of power is absorbed by the electrons (48% at $d = 5$ mm), the less power absorbed by the Xe_2^+ (35% at $d = 5$ mm) and approximately the same power absorbed by the Xe^+ (16% at $d = 5$ mm). In other words, increasing gap distance is beneficial to VUV emission because of the increasing electron power absorption (12.5–47.7%) and the reduced ion power absorption (87.5–52.3%).

Figure 11a, b show the spatial distributions of cycle averaged VUV emission and power deposition through electrons and ions across the gap, respectively. It can be found spatial distribution of power density P_{172} correlates very well with that of power density of P_e. Also, the peak value of power density of P_{172} in the bulk region (near the sheath edge)

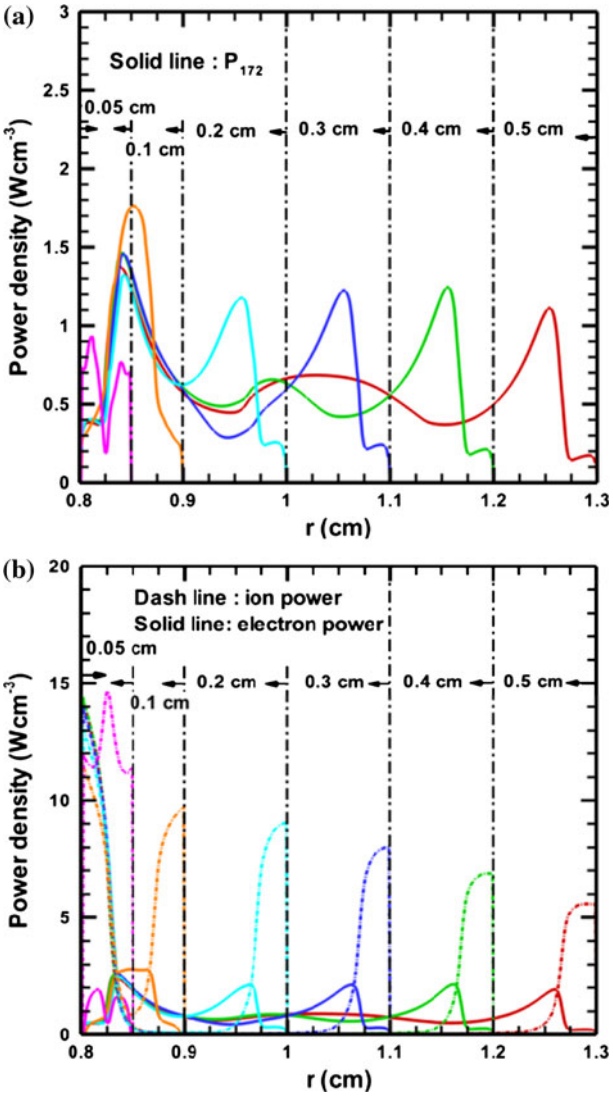

Fig. 11 Spatial distribution of cycle-averaged power densities at different gap distances: **a** VUC emission and **b** ions and electron

remains approximately the same for all different gap distances (Fig. 11a). Similar trends are also observed for power density of P_e (Fig. 11b). It is thus clear that the increase of P_{172} as well as P_e with increasing gap distance, as shown in Fig. 10, is attributed to the "volumetric integral" effect in the larger outer cathode and wider bulk region. Interestingly, Fig. 11b shows that the power density absorbed through ions ($P_{Xe^+} + P_{Xe_2^+}$) in the outer sheath decreases with increasing gap distance because of reduced applied electric field, while the power densities absorbed through ions in the inner sheath remains approximately the same. However, the total powers absorbed through ions remain approximately the same at different gap distances, as shown earlier in Fig. 10b, also because of the "volumetric integral" effect as mentioned in the above. One exception is the case with a gap distance of 0.5 mm, which the plasma is a typical Townsend-like discharge that there are much fewer electrons than the ions across the gap in general, in which the details of the discharge are not described here.

Effect of Varying the Number of Dielectric Layers

Figure 12a shows that the values of η_{172}, P_{tot} and P_{172} for the cases with one- and two-dielectric layers, while Fig. 12b shows the corresponding power partitions among different charged species. It is clearly that all η_{172}, P_{tot} and P_{172} of the two-dielectric case are larger than those of one-dielectric one. P_e increases from a value of 188 W in the two-dielectric case is up to 637.3 W in the one-dielectric case, which results in the increase of P_{172} from 122.3 W to 453.3 W. However, the growth of P_{ion} (= $P_{Xe^+} + P_{Xe_2^+}$) from 244.2 W in the two-dielectric case to 719.3 W in one-dielectric case results in more wasted power in ion heating, although the increase of η_{172} can increase from 28.9 to 33.5%. Interestingly, Fig. 12c shows the power partitioning in P_{tot} for the one- and two-dielectric cases remains approximately the same.

Figure 13a, b show the spatial distributions of cycle averaged electric field and power deposition through charged species across the gap, respectively, for the one- and two-dielectric cases. Figure 13a shows that electric field at the inner side for the one-dielectric case is 1.33 times larger than that for the two-dielectric one. This is caused by the fact that the applied voltage in the one-dielectric case can be directly applied to the discharge without the shielding of accumulated charged species at the dielectric surface if there is dielectric layer at the inner side. This is reflected in the ultra high value of power density absorbed through ions at the inner sheath, as shown in Fig. 13b. However, use of one-dielectric in the xenon DBD may have other negative side effects. For example, inner electrode surface may be quickly eroded by the bombarding of highly energetic ions because of this very large electric field. Thus, two dielectric layers are generally used in practice.

Conclusion

In this paper, the detailed process of VUV emission and power deposition of charged species for a coaxial excimer xenon lamp driven by 50 kHz distorted bipolar square voltages has been investigated numerically. A self-consistent radial one-dimensional fluid model considering local mean energy approximation is employed to simulate the complicated discharge physics and chemistry. The process is divided into two portions of three breakdown periods, which include the pre-discharge, the discharge (most intense 172 nm

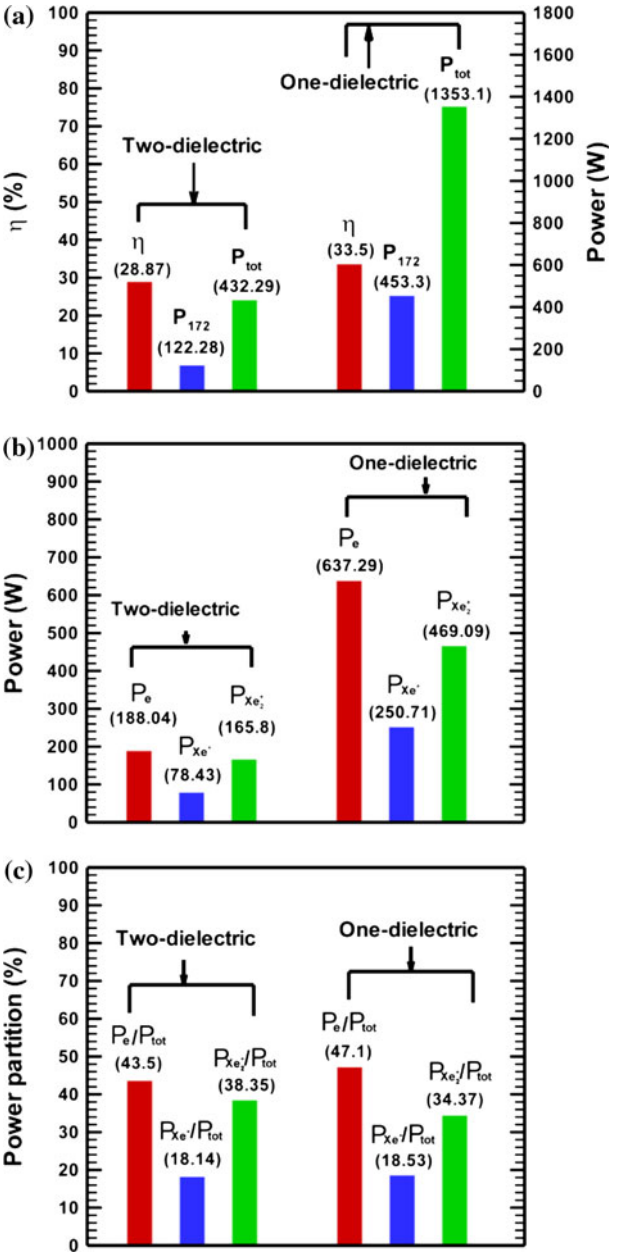

Fig. 12 Effect of number of dielectric materials on: **a** P_{tot} and P_{172}, **b** power deposition of various charged species, and c) fraction of power deposition for different charged species at 50 kHz of power source, 400 torr of gas pressure and 4.5 mm of gap distance

VUV emission) and the post-discharge periods. The results show that electron power deposition occurs mainly in the early portion of discharge period (period II-1 and V-1) in which the VUV emission is most intense, while Xe^+ and Xe_2^+ power depositions occur in

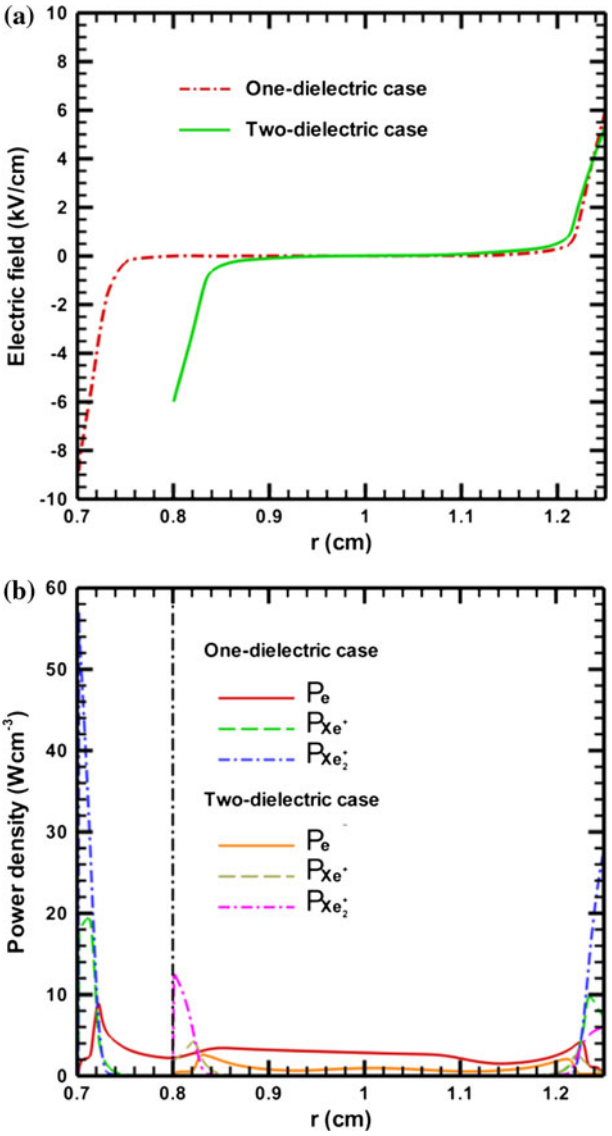

Fig. 13 Spatial distribution of cycle averaged properties for one and two dielectric cases: **a** electric field and **b** power densities of charged species at 50 kHz of power source, 400 torr of gas pressure and 4.5 mm of gap distance

the whole discharge period (period II and V) and later part of discharge period (period II-2 and V-2), respectively.

Extensive parametric study of the VUV emission (172 nm) from the same excimer xenon lamp by varying the four key parameters (frequency, pressure, gap distance and number of dielectric) has also been investigated. The results show that: 1) the effect of varying frequency is minimal; 2) a maximal value of VUV emission exists at 600 torr; 3)

VUV emission increases with increasing gap distance and 4) the value of VUV emission in the case of one-dielectric case is better than two-dielectric, although inner electrode surface may be quickly eroded by the bombarding of highly energetic ions because of the very large electric field.

Acknowledgments The authors would like to thank the financial support by the National Science Council of Taiwan (NSC 96-2628-E-009-134-MY3), ITRI/MCL through Dr. Bee-Yu Wei, Institute of Nuclear Energy Research (992001INER028), and Ministry of Economic Affairs of Taiwan.

References

1. Beleznai S, Mihajlik G, Agod A, Maros I, Juhasz R, Nemeth Z, Jakab L, Richer P (2006) J Phys D Appl Phys 39:3777
2. Bolsig, http://www.siglo-kinema.com/bolsig.htm
3. Cai XC, Casarin MA, Elliott FW, Widlund OB (1998) Contemporary mathematics. American Mathematical Society, Boulder
4. Carman RJ, Mildren RP (2003) J Phys D Appl Phys 36:19
5. Hung CT, Hu MH, Wu JS, Hwang FN, Hwang FN (2007) Comput Phys Comm 177:138
6. Hung CT, Hu MH, Wu JS, Hwang FN (2010) Comput Phys Comm (accepted)
7. Eliasson B, Kogelschatz U (1988) Appl Phys B 46:299
8. Grubert GK, Becker MM, Loffhagen D (2009) Phys Rev E 80(3):36–405
9. Kane DM, Hirschausen D, Ward BK, Carman RJ, Mildren RP (2004) Proc ShPIE 5399:100
10. Oda A, Sakai Y, Akashi H, Sugawara H (1999) J Phys D Appl Phys 32:2726
11. Park JH, Lee IK, Cho BH, Lee JK, Whang KW (2007) *PCC'07* 717
12. Safta E (2004) US Patent 6,767,458
13. Shiga T, Mikoshiba S, Shinada S (2001) Elec Comm Japan 84:55
14. Stockwald S, Neiger M (1995) Contrib Plasma Phys 35:15
15. Vollkommer F, Hitzschke L (1997) US Patent 5,604,410